Modeling and Simulation of Unsteady Flow in Multistage Compressors Using Interdomain Boundaries

Yedidia Neumeier,* Abhishek Mishra,† and J. V. R. Prasad‡
Georgia Institute of Technology, Atlanta, Georgia 30332
and
Darrell K. James§
Honeywell International, Inc., Phoenix, Arizona 85034

https://doi.org/10.2514/1.B38414

In this paper, a model for simulating the intrinsic fast dynamics of flow in a multistage, axi-centrifugal compressor is presented. The model treats the flow through the stage elements, i.e., rotors and stators, as curved stream-tube elements along the mean line. The model captures unsteady flow dynamics in respective frames for stators and rotors of individual stages, alternating between stationary and rotating frames as needed. Accelerations associated with the rotating frames are represented as body forces. Unique characteristics-based compact interfaces that account for the transformations between the frames (and also serve as compact loss zones) are used. Simulation results for an industrial four-stage axial compressor are presented that illustrate the propagation of waves through the compressor segments as the throttle is moved. In particular, the dynamic processes that can lead a compressor to either of the opposite ends of its operation, i.e., loss of stability or choked flow, are investigated. Simulation results demonstrate that the model accounts for the acoustic impedance that is responsible for choked flow. In throttling toward stall, the simulation results show, as expected, that with large plenum the compressor loses stability when it is driven beyond the peak of its characteristics. Further, the capabilities of the developed model as a diagnostic tool are demonstrated by analyzing "pseudomeasured" pressure signals in two possible scenarios of stability loss.

Nomenclature

A	=	cross-sectional area
Cp	=	specific heat at constant pressure
C_Q	=	heat source term
e_0	=	total internal energy
F_{dis}	=	dissipation force per unit length
h_0	=	stagnation enthalpy
M	=	Mach number
m	=	mean line
$\dot{m}$	=	mass flow rate
$\boldsymbol{m}$	=	unit vector tangent to mean line
$\boldsymbol{n}_m$	=	unit vector binormal to mean line
$\boldsymbol{n}_r$	=	unit vector normal to mean line
p	=	pressure
R	=	gas constant r radius
T	=	temperature
t	=	time
V	=	velocity along mean line
α	=	angle of attack
β	=	circumferential inclination angle of mean line
γ	=	specific heat ratio; also radial inclination angle of mean line
ρ	=	fluid density
Ω	=	angular shaft speed

Subscripts

cen	=	centrifugal
cor	=	Coriolis
m	=	along mean line
n	=	normal to mean line

Presented as Paper 2018-4826 at the 2018 AIAA Joint Propulsion Conference, Cincinnati, OH, January 9–11, 2018; received 8 February 2021; revision received 12 November 2021; accepted for publication 22 December 2021; published online 31 January 2022.

*Retired Research Professor, School of Aerospace Engineering (Corresponding Author).
†Ph.D. Graduate, School of Aerospace Engineering.
‡Professor, School of Aerospace Engineering. Fellow AIAA.
§Fan and Compressor Methods Staff Engineer.

I. Introduction

MEAN-LINE flow models for design point and off-design operation performance analysis are common tools in compressor design [1–3]. With advances in computational fluid dynamics (CFD) over the years, usage of mean-line models is often restricted to early stages of a design, leaving the detailed design for more sophisticated CFD tools. However, mean-line flow models offer computational advantage in simulating the fast dynamic of compressible flow in a compressor, which can become very useful in compressor design trade studies.

Reduced-order models for dynamic analysis of flow in a compressor, typically, analyze the entire compressor as a lumped object and use a heuristic force function that "pushes" the flow against adverse pressure. The force function is obtained indirectly from the compressor characteristics that are obtained from tests, or alternatively, from CFD analysis. The usefulness of the heuristic force function approach was well demonstrated by Greitzer [4,5]. The lumped parameters model studied by Greitzer consisted of a compact pump/compressor that generated pressure in response to the flow through it. The compact pump discharged into a cavity that was coupled at the other end to a plenum, the exit of which was interfaced to the ambient through a throttle. In this model, fluid in the cavity acted as a lumped mass, and all the compressible effects took place in the plenum only. Even with these simplistic assumptions, the model is quite useful in predicting basic stability criterion, and importantly, it introduces the well-known B-parameter. Furthermore, using the same force function approach combined with incompressible flow in the compressor passages, Moore [6] developed a comprehensive model for the rotating stall. Thus, it was a natural next step to use the force function approach and relax the incompressible flow assumption so that compressibility could be accounted for in the compressor cavity.

Longley [7] developed a novel approach for simulating the moderate to long length-scale compressible unsteady flowfield within a compression system. Léonard and Adam [8] formulated the time-dependent equations of flow through a compressor, and included distributed blade forces in the momentum equation as a source in the same way that body

force would be accounted for. However, there were no transient response results presented in the paper by Léonard and Adam [8]. Dhingra et al. [9] used a similar approach to examine the possibility of identifying the stalling stage via the mechanism of compression and expansion waves that emanate from the stalling stage.

Although the distributed blade force [8,9] described above may be of some benefit, it cannot properly capture the details of wave propagation in a compressor. Firstly, the individual stage passages are not oriented along the compressor shaft axis, rather they are staggered, and therefore waves propagating along a pure axial flow would have to "penetrate" through the blades. Furthermore, the actual Mach number in a staggered stage passage is significantly higher than that of its axial flow component. Finally, it is important to note that the relative rotation, turning losses, and possible choking play a key role in determining the acoustic impedance that is responsible for transmission and reflection of pressure waves at the interfaces between the rotors and stators. These effects cannot be simulated with a model that assumes axial flow with distributed blade forces. In contrast, the approach presented in this paper solves the compressible flow as it makes its way through the "actual" passages in the blade cascades, and it accounts for a realistic acoustic impedance between stators and rotors. Assuming infinitely thin blades, it turns out that the force extracted through the pressure on the blade surface is chiefly perpendicular to the mean stream line. Thus, in our approach, no other force, besides retarding forces such as wall friction, comes into account in the unsteady flow in its corresponding stream tube. The "push" to the flow appears through the addition of apparent velocity at the junctions between the rotors and stators. The approach can be broadly described as presenting the operation of the compressor in terms of successive diffusers with velocity addition at the junctions between the rotors and stators as illustrated in Fig. 1. Specifically, when we switch between rotating and stationary frames of reference in our observation of flow, a lateral velocity U appears in the observer frame of reference, whereas the axial and radial components of flow velocity as well as pressure, density, and temperature are unaffected. It is important to note that the addition of lateral velocity changes the direction of flow that, in turn, changes the cross-sectional area of the stream tube such that mass flow rate is continuous through the interface as illustrated in Fig. 1.

One may wonder if this approach can really capture the actual dynamics of flow in a compressor. As seen from simulation results presented in the latter part of the paper, flow accelerates and decelerates in response to throttle changes in a "real" fashion as would be observed during tests, thus establishing that the scheme in Fig. 1 can be used for simulations of steady and transient behaviors of flow inside a compressor.

To facilitate a numerical solution of the model shown in the above scheme, it is required for the numerical scheme to alternate between rotating and nonrotating frames. This, in turn, requires dynamic interfaces to serve as boundaries between two computational domains. To that end, a novel characteristics-based interface framework is developed. Finally, to obtain a realistic model, it is necessary to calculate the losses associated with extra entropy generation in the flow process. Losses are mostly governed by complicated 3-D flows in which kinetic energy of the fluid is converted to heat via internal dissipation. Therefore, incorporating losses in mean-line models, which are essentially restricted to 1-D flow, is known to be tricky and requires a combination of good physical understanding and correlation with large amount of data such as reported by Lieblein et al. [10] and Lieblein [11]. The reader will find a good narrative of this subject in the paper by Smith and Koch [12] and in the IGTI Scholar lecture by Denton [13]. Both references underscore the difficulties of modeling losses in transient flow simulations. Denton emphasizes the advantage of phenomenological loss models that can capture the global physics of the losses while ignoring the finer details. It is understood that the challenge involved in loss models that can be incorporated in a dynamic model is more complex because of the need to incorporate loss terms into the differential equations rather than accounting for losses over the entire stage. As an example, the losses due to blade tip leakage can be relatively easily estimated but are not readily incorporated in the formulation of 1-D unsteady flow equations. Thus, when 1-D unsteady flow is considered, we cannot readily apply classical loss formulas such as proposed by Lieblein et al. [10] and Lieblein [11]. The method used to incorporate different types of losses in our model is described in detail in [14]. Using this method, it is shown in Ref. [14] that the model recovers measured compressor characteristics accurately over a large range of speeds. This success formed the basis for its use in the current study of unsteady flow in a compressor.

At the expense of repetition, we want to highlight that the mean-line unsteady flow model presented in the current work captures the progression of pressure waves as they travel through the *staggered conduits* formed by the blade cascade passages during transients including stall and choke. This is in contrast to the models developed in [8,9], which considered axial flow with distributed body forces representing the axial component of blade aerodynamic forces. The model implementation requires alternating between stationary and rotating frames across stages, which, in turn, requires interfaces between computational domains. To that end, a novel treatment of the corresponding interfaces between blade rows has been developed.

The remainder of the paper is organized as follows: First, we provide details of the model development followed by a description of the numerical scheme used for simulation. Then, we present simulation results illustrating details of the wave dynamics through the compressor as a mechanical throttle is used to vary the flow rate through the compressor, particularly as the system is throttled into a stall or a choke condition. At the end, we provide a list of conclusions that are drawn from the results presented.

II. Mean-Line Construction and Flow Equations

A. Mean-Line Considerations

We consider mean-line m (m-line), which is the trajectory of the bulk flow through a stream-tube element defined by the passage between two blades. We consider axisymmetric flow geometry; thus, the mean-line trajectory lies on a surface of revolution. At each point on the trajectory, we position a plane that is tangent to the surface, and another plane that contains the axis of rotation (the spool axis). An overlay of these radial planes would yield collections of points like the dotted line shown in Fig. 2. Note that each point is located at a distance r from the rotation axis. The orientation of the unit vector at a point along the mean line is defined by two successive rotations, the first rotation about $\boldsymbol{k}$ by the radial inclination angle γ and the second rotation about $\boldsymbol{j}'$ by the circumferential inclination angle β, as shown in Fig. 2. Additionally, a point along the mean line is associated with a cross-sectional area A, which represents the area of the surrounding stream tube, and a characteristic width b, which represents the shape factor of the surrounding stream tube. We now derive the equation of the m-line as follows.

First, consider the radial plane that contains a point on the mean line, the plane consisting of the rotation axis x and radial coordinate y with corresponding unit vectors $\boldsymbol{i}$ and $\boldsymbol{j}$, respectively. The z direction with corresponding unit vector $\boldsymbol{k}$, according to the right-hand rule, is pointing outward perpendicular to the xy plane. Next, we consider a

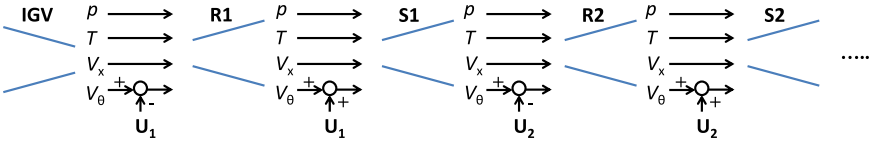

Fig. 1 Flow schematic showing multistage axial compressor modeled as successive diffusers with velocity addition junctions.

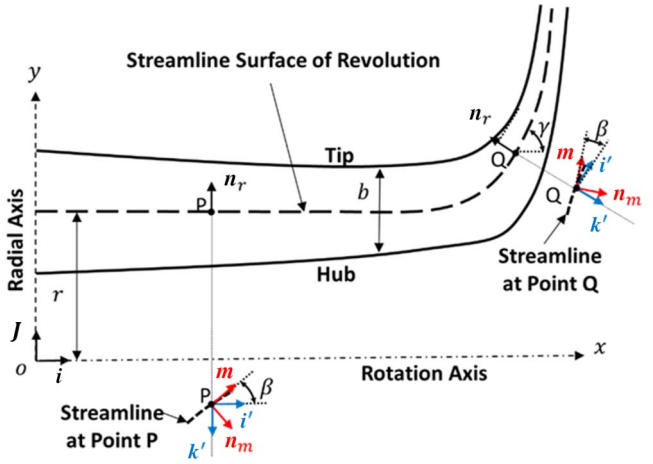

Fig. 2 Geometric and vector notation.

plane tangent to the surface of revolution that contains the said mean-line point of the m-line whose unit vectors are $\boldsymbol{i}'$, $\boldsymbol{j}'$, and $\boldsymbol{k}'$, and its area vector $\boldsymbol{n}_r$ is, thus, projected on the corresponding plane xy and is tilted by the angle γ from the radial axis y. Note that when $\gamma = 0$, $\boldsymbol{i}' = \boldsymbol{i}$, $\boldsymbol{j}' = \boldsymbol{j}$, and $\boldsymbol{k}' = \boldsymbol{k}$. We now consider the unit vector $\boldsymbol{m}$ that is tangent to the line m at the corresponding point and lies on the plane $\boldsymbol{i}'\boldsymbol{k}'$ at an angle equal to the circumferential inclination angle β. This vector overlaid on the trace of m is shown in the bottom part of Fig. 2 at two locations (shown as points P and Q) along the axial-centrifugal compressor: point P represents mostly axial flow corresponding to an axial stage, and point Q represents mixed axial-radial flow corresponding to a centrifugal stage.

From Fig. 2, we can represent $\boldsymbol{m}$ in terms of $\boldsymbol{i}'$ and $\boldsymbol{k}'$ as

$$\boldsymbol{m} = \cos\beta\boldsymbol{i}' - \sin\beta\boldsymbol{k}' \tag{1}$$

Since the vector $\boldsymbol{j}'$ is normal to $\boldsymbol{m}$, we can thus calculate the third vector in the streamline system $\boldsymbol{n}_m = \boldsymbol{m} \times \boldsymbol{j}'$, which gives

$$\boldsymbol{n}_m = \sin\beta\boldsymbol{i}' + \cos\beta\boldsymbol{k}' \tag{2}$$

Further, it can be easily observed that

$$\begin{aligned}\boldsymbol{i}' &= \cos\gamma\ \boldsymbol{i} + \sin\gamma\ \boldsymbol{j}\\ \boldsymbol{j}' &= -\sin\gamma\ \boldsymbol{i} + \cos\gamma\ \boldsymbol{j}\\ \boldsymbol{k}' &= \boldsymbol{k}\end{aligned} \tag{3}$$

Substituting Eq. (3) into Eqs. (1) and (2) gives

$$\begin{aligned}\boldsymbol{m} &= \cos\beta\cos\gamma\ \boldsymbol{i} + \cos\beta\sin\gamma\ \boldsymbol{j} - \sin\beta\ \boldsymbol{k}\\ \boldsymbol{n}_m &= \sin\beta\cos\gamma\ \boldsymbol{i} + \sin\beta\sin\gamma\ \boldsymbol{j} + \cos\beta\ \boldsymbol{k}\end{aligned} \tag{4}$$

It can be verified that the magnitude of each unit vectors $\boldsymbol{m}$ and $\boldsymbol{n}_m$ is unity.

$$\begin{aligned}|\boldsymbol{m}| &= \sqrt{\cos^2\beta\cos^2\gamma + \cos^2\beta\sin^2\gamma + \sin^2\beta} = 1\\ |\boldsymbol{n}_m| &= \sqrt{\sin^2\beta\cos^2\gamma + \sin^2\beta\sin^2\gamma + \cos^2\beta} = 1\end{aligned} \tag{5}$$

Now, let us scale the mean-line unit vector $\boldsymbol{m}$ by multiplying both sides of Eq. (4) by dm, and denote $\mathrm{d}m\ \boldsymbol{m} = \boldsymbol{dm}$.

$$\boldsymbol{dm} = \cos\beta\cos\gamma dm\ \boldsymbol{i} + \cos\beta\sin\gamma dm\ \boldsymbol{j} - \sin\beta dm\ \boldsymbol{k} \tag{6}$$

On the other hand, we can also represent mean-line differential vector in terms of Cartesian variables:

$$\boldsymbol{dm} = dx\ \boldsymbol{i} + dy\ \boldsymbol{j} + dz\ \boldsymbol{k} \tag{7}$$

Comparing Eqs. (6) and (7) and noting that $dy = dr$, we get

$$\begin{aligned}\mathrm{d}m &= \frac{dx}{\cos\beta\cos\gamma}\\ \mathrm{d}m &= \frac{dr}{\cos\beta\sin\gamma}\end{aligned} \tag{8}$$

In the axial part, where the angle γ is close or equal to zero, we express everything as a function of x, namely, $r(x)$, $\gamma(x)$, and $\beta(x)$, and we use the formula from the upper part of Eq. (8). In the radial part, where γ approaches 90 deg, we replace x by r as the independent variable such that $x(r)$, $\gamma(r)$, and $\beta(r)$, and we use the formula from the lower part of Eq. (8). The angle $\gamma = 45$ deg is chosen as the switching inclination angle. After integrating Eq. (8), we can determine the geometrical variables as functions of m, namely, $r(m)$, $\gamma(m)$, and $\beta(m)$, which with the corresponding mean-line area $A(m)$ can be used in the formulation of the mean-line flow equations as shown next.

B. Flow Governing Equations

In some sections of the compressor, the m-line is attached to a stationary row (inlet duct, inlet guide vanes, stator, diffuser section), and in other sections, it is in a noninertial rotating frame attached to the rotor. The rotating frame introduces inertial forces on fluid particles, namely, the centrifugal force and Coriolis force. The centripetal acceleration is in the direction of $-\boldsymbol{j}$ and its magnitude is $\Omega^2 r$.

The force components per unit mass along and normalto $\boldsymbol{m}$ are given by

$$\begin{aligned}F_{\mathrm{cen},\boldsymbol{m}} &= \Omega^2 r\boldsymbol{j}\cdot\boldsymbol{m} = \Omega^2 r\cos\beta\sin\gamma\\ F_{\mathrm{cen},\boldsymbol{n}_m} &= \Omega^2 r\boldsymbol{j}\cdot\boldsymbol{n}_m = \Omega^2 r\sin\beta\sin\gamma\end{aligned} \tag{9}$$

The Coriolis force per unit mass is given by

$$\boldsymbol{F}_{\mathrm{Cor}} = -2\boldsymbol{\Omega}\times\boldsymbol{V} = -2\Omega V(\boldsymbol{i}\times\boldsymbol{m}) = -2\Omega V(\sin\beta\boldsymbol{j} + \cos\beta\sin\gamma\boldsymbol{k}) \tag{10}$$

where V is the magnitude of flow velocity along the mean line. The cross product $\boldsymbol{\Omega}\times\boldsymbol{V}$ implies that the resultant force is perpendicular to both $\boldsymbol{\Omega}$ and $\boldsymbol{V}$. Since $\boldsymbol{V}$ is oriented along $\boldsymbol{m}$, the Coriolis force has no component along $\boldsymbol{m}$. The component normal to $\boldsymbol{m}$ along $\boldsymbol{n}_m$ is

$$F_{\mathrm{cor},\boldsymbol{n}_m} = -2\Omega V\sin\gamma \tag{11}$$

Note that the Coriolis effect is null when $\gamma = 0$ and is maximum in pure radial flow when $\gamma = 90$ deg.

We now apply the conservation laws with source terms to obtain the governing equations.

Continuity:

$$\frac{\partial(\rho A)}{\partial t} + \frac{\partial(\rho VA)}{\partial m} = 0 \tag{12}$$

Energy:

$$\frac{\partial(\rho e_0 A)}{\partial t} + \frac{\partial(\rho V h_0 A)}{\partial m} = \rho VA\Omega^2 r\cos\beta\sin\gamma - C_Q \tag{13}$$

Momentum along the mean line:

$$\frac{\partial(\rho VA)}{\partial t} + \frac{\partial(\rho V^2 A)}{\partial m} = -A\frac{\partial p}{\partial m} + \rho A\Omega^2 r\cos\beta\sin\gamma - F_{\mathrm{dis}} \tag{14}$$

where C_Q represents the heat loss due to cooling, F_{dis} is a dissipating force source term that brings into effect the distributed losses due to

wall friction as well as tip leak and other sources,[¶] Ω is the compressor shaft angular speed, γ is the radial inclination of mean line, and e_0 and h_0 are total energy and stagnation enthalpy, respectively, defined as

$$e_0 = \frac{p}{\rho(\gamma - 1)} + \frac{1}{2}V^2$$
$$h_0 = h + \frac{1}{2}V^2 \tag{15}$$

In addition to the above equations, we also use the perfect gas law to relate the thermodynamic variables

$$p = \rho RT \tag{16}$$

Equations (12–16) are applicable to any configuration that is encountered in a compressor, be it pure axial, centrifugal, or mixed axial-centrifugal.

Considering now the energy equation without time derivatives and assuming no heat losses, we get

$$\frac{\partial(\rho V h_0 A)}{\partial m} = \rho V A \Omega^2 r \cos\beta \sin\gamma \tag{17}$$

Equation (17) shows that in an adiabatic pure axial stage where $\gamma = 0$ deg (i.e., the radius of the mean line is constant), the total enthalpy (as measured in the corresponding stage relative frame of reference) is constant along the stage, i.e.,

$$\rho V h_0 A = \text{constant} \tag{18}$$

On the other hand, in a radial impeller where $\gamma = 90$ deg, there is a total enthalpy increase as a result of the work done by the centrifugal forces. For the four-stage axial compressor considered for transient simulations in this study, we take the mean-line radial inclination angle γ to be zero, thus having no contribution from the centrifugal force source terms.

The formulation of the flow Eqs. (12–14) assumes that the observer is fixed to the corresponding blade row, thus making the observer stationary with respect to the flow path. This approach works as long as we transform the flow variables correctly when we switch between rotating and nonrotating frames of reference. The validity of this approach is undisputed as rotating frames of reference are routinely used in the development of flow equations, and the simplicity it brings to the flow equations is evident. However, this very simplification can be a potential source for confusion. One may find it hard to grasp the disappearance of the aerodynamic force terms in the momentum equation, as seen from Eq. (14). Further, as there is no inclusion of work done by aerodynamic force in the energy equation [see Eq. (13)], the total enthalpy in the blade row channel does not change. This begs the following question: How the increase in the flow enthalpy between the inlet and the outlet is accounted for in the current model?

The answer to the latter question is that a change in enthalpy appears as a jump when we switch between reference systems due to the apparent velocity addition. As we switch back, there is another jump, and the net difference between the jumps provides a change in total enthalpy. Thus, for an observer moving with the conduit flow, enthalpy along the compressor appears to increase in steps. If we transform the calculated flow variables to the inertial system, we will notice that the calculated enthalpy increases gradually along the compressor.

The first question concerning the disappearance of the aerodynamic force term from the momentum equation can be elucidated using the go-through assumption that is often used to explain the modal rotating stall [15] as follows: Consider a 1-D axial flow in a compressor with constant area cavity modeled as parallel *straight* stream tubes extending along the compressor cavity, interrupted at various locations by a compact blade section representing a rotor or a stator. The go-through assumption suggests that the flow entering a blade row goes straight through it, but gains or loses pressure due to the action of aerodynamic forces from the blades. In this case, the momentum balance of the stream tube must contain a force term that pertains to the aerodynamic force from the blades, which is responsible for the pressure increase along the compressor. Note that blades are located at discrete points along the flow path. Thus, as one follows a stream line, a pulse of force appears in the momentum equation at the point where the streamline "goes through" the blade actuator, with no forces appearing at points in between the blades. In contrast, in the *curved* mean-line modeling approach pursued in this work, there are no intersections with the blades, and thus, there is no force term along the flow path. It should be noted, however, that there is a force term in the momentum equation in the lateral direction. This force "causes" the flow to follow the conduit between the blades. This auxiliary equation is not needed for our solution of the flow; it can be solved to obtain the aerodynamic blade forces that are required for the conduit flow.

Yet, another point that may be a source of confusion is the continuity of mass flow rate across the transformations. The velocity addition at the interfaces of blade rows gives the false notion that mass sources are introduced. As we switch between rotating frames, the flow properties such as density ρ, pressure p, and temperature T do not change. However, the flow velocity V is changed due to blade rotation when viewed by an observer in the rotating frame. However, a geometrical consideration of the resulting curved stream tube implies that the cross-sectional area A of the stream tube jumps as well in such a way that it keeps the mass flow rate ρVA continuous when we switch between rotating and nonrotating frames. This jump in the area is depicted schematically in Fig. 1.

C. Steady-State Model Highlights

The validity of our model simulations is based on the premise that steady-state solutions of the model correlate well with the real characteristics of the simulated compressor. With this premise being a necessary condition for this work, we bring below, for the benefit of the reader, some highlights from [14], which includes a detailed description of steady-state solutions of the model and correlations with the measured data for an industrial four-stage axial compressor.

1. *Losses Consideration*

When flow enters a stage with zero incident angle, it follows the mean line all along. However, when significant incident angle develops, flow is forced to turn sharply at the entrance to the blade cascade passage before it is realigned with the mean line of the cascade. This turning is treated in the model as an abrupt expansion (positive incidence) or contraction (negative incidence) in the stream tube area, as shown in Fig. 3. This source of losses may be somewhat pessimistic

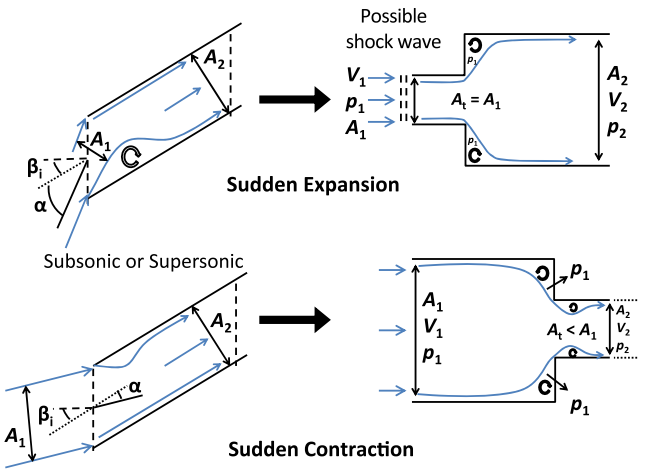

Fig. 3 Flow entering the blade row at positive angle of attack shown as sudden expansion (top figure), whereas the stream entering at negative angle of attack is represented as sudden contraction (bottom figure).

[¶]One may wonder why the term F_{dis} does not have a contribution to the energy equation. Indeed, dissipative forces do not appear in the energy equation; see, for example, the derivation of Fanno flow equations. A full discussion of this subject is important on its own, but it is beyond the scope of the current paper.

at low angles of attacks, but our results in [14] suggest that this model provides reasonable estimates of losses at larger angles of attack. Other losses such as tip leak and boundary-layer viscous effects are included using the term F_{dis} in the momentum equation [see Eq. (14)].

2. Flow Deviation Consideration

The essence of deviation can be understood by comparing a cascade flow when blades are far from each other (low solidity) to a cascade flow where the blades are very close, thus forming a tight conduit (high solidity). In the first case, flow changes direction only in the vicinity of the blades, leaving the bulk flow to continue in its upstream direction. In this case, the bulk flow deviates from the orientation of the blade. In the latter case, flow is forced to follow the conduit direction with little deviation. It is thus expected that the deviation of the bulk flow is an inverse function of solidity. Further details on how flow deviation is accounted for in the current model can be found in [14].

3. Steady-State Model Correlations

A comparison of the steady-state model predictions with the measured data for an industrial four-stage axial compressor is shown in Fig. 4, which is taken from [14]. The same set of parameters used for calibration of the steady-state model in [14] is used for unsteady flow simulations in the current paper.

III. Numerical Solution and the Dynamic Compact Interfaces

A. Numerical Scheme

We consider the system of partial differential equations (PDEs) given in Eqs. (12–14) in a canonical conservative form:

$$\frac{\partial U}{\partial t} + \frac{\partial F(U)}{\partial m} = Q(U) \tag{19}$$

where

$$U = \begin{bmatrix} \rho A \\ \rho V A \\ \rho e_0 A \end{bmatrix}, \quad F = \begin{bmatrix} \rho V A \\ \rho V^2 A + pA \\ \rho V h_0 A \end{bmatrix},$$

$$Q = \begin{bmatrix} 0 \\ p\frac{\partial A}{\partial m} + \rho A \Omega^2 r \cos\beta \sin\gamma - F_{\text{dis}} \\ \rho V A \Omega^2 r \cos\beta \sin\gamma - C_Q \end{bmatrix}$$

Riemann solvers that follow the eigenvalues or characteristic velocities of the flow equations and the corresponding eigenvectors are naturally suitable for the solution of Eq. (19). However, due to the inherent complexities of the iterative procedure required for finding the eigenvectors, approximate Riemann solvers such as Roe and Harten-Lax-van Leer (HLL) solvers became more popular [16]. Roe solver is very robust and has high resolution near shock discontinuities. Modifications to the Roe scheme for inclusion of source terms were established by Mohanraj et al. [17]. Still, finding the eigenvectors of the linearized Jacobian matrix involves significant computational effort. In contrast, Riemann-solver-free central schemes that rely on flux updates directly in terms of physical fluxes are straightforward, and thus are computationally alluring. The first stable such central scheme was introduced by Lax [18], but it had a low resolution. Significant modifications by Kurganov and Tadmor (KT) second-order accuracy scheme [19] enabled high resolution, while keeping the advantages of simplicity and computational efficiency of the central scheme. The so-called second-order KT scheme can be used in fully discrete form, that is, converting the PDEs directly into algebraic equations, or semidiscrete form in which the PDEs are first converted into ordinary differential equations (ODEs), which are subsequently integrated. In our numerical scheme, we follow the latter approach. We provide a brief description of the numerical scheme below.

The semidiscretized form of the conservation law using central differencing can be expressed as

$$\frac{\partial U_j}{\partial t} = -\frac{H_{j+1/2} - H_{j-1/2}}{\Delta m_{j,c}} + Q(U_j) \tag{20}$$

with the spatial grid size calculated using central differences:

$$\Delta m_{j,c} = \frac{m_{j+1} - m_{j-1}}{2}$$

The "numerical flux" H that replaces the "physical flux" F is calculated as follows:

$$H_{j+1/2} = \frac{1}{2}\left(F\left(U^+_{j+1/2}\right) + F\left(U^-_{j+1/2}\right)\right) - \frac{a_{j+1/2}}{2}\left(U^+_{j+1/2} - U^-_{j+1/2}\right) \tag{21}$$

with the corresponding term $H_{j-1/2}$ calculated similarly by replacing $j + 1/2$ with $j - 1/2$ in Eq. (21) and $a_{j+1/2}$ is the maximum local wave speed given by

$$a_{j+1/2} = \max\left\{\left|V^+_{j+1/2} + c^+_{j+1/2}\right|, \left|V^+_{j+1/2} - c^+_{j+1/2}\right|, \left|V^-_{j+1/2} + c^-_{j+1/2}\right|, \left|V^-_{j+1/2} - c^-_{j+1/2}\right|\right\} \tag{22}$$

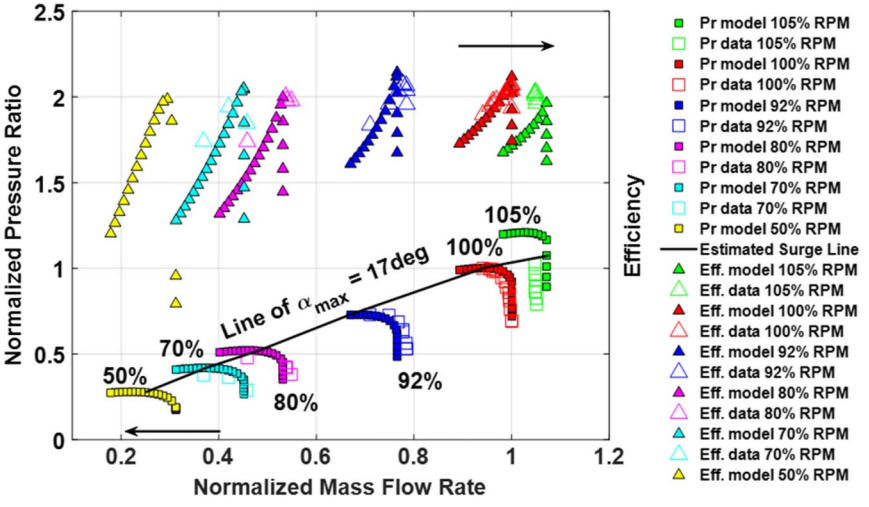

Fig. 4 Measured and predicted pressure ratios and efficiencies at various compressor speeds.

In the above, the "right" $[\ ]^{+}_{j+(1/2)}$ and the "left" $[\ ]^{-}_{j+(1/2)}$ operators of any of the grid variables Y_j (e.g., U_j, V_j) are linearly reconstructed variables at $j + 1/2$ location corresponding to $j + 1$th and jth cells, respectively, as shown below:

$$Y^{+}_{j+(1/2)} = Y_{j+1} - S_{j+1}\frac{\Delta m_{j+1,c}}{2}$$
$$Y^{-}_{j+(1/2)} = Y_j + S_j\frac{\Delta m_{j,c}}{2} \tag{23}$$

in which the derivatives S_{j+1} and S_j are determined with minmod limiter of van Leer's one-parameter family.

$$S_j = \text{minmod}\left(\theta\frac{Y_j - Y_{j-1}}{m_j - m_{j-1}}, \frac{Y_{j+1} - Y_{j-1}}{m_{j+1} - m_{j-1}}, \theta\frac{Y_{j+1} - Y_j}{m_{j+1} - m_j}\right),$$
$$\text{where } \theta \in [1, 2] \tag{24}$$

The minmod operator returns the term with minimum magnitude along with its sign if all terms have the same sign, and returns zero otherwise. θ is the dissipation parameter, and can be varied from 1 to 2. When $\theta = 1$, and assuming that all terms share the same sign, the minmod chooses the least amplitude derivative resulting in damping of the spurious oscillations, but enhancing numerical diffusion. With larger values of θ, the minmod delivers a derivative larger in magnitude than the minimum, but always lesser in magnitude than that based upon the central difference. This in turn lessens the numerical damping, bounded by the least diffusive central difference term.

After explicit calculation of the flux and the source terms at each time step, we integrate the semidiscrete formulation, i.e., Eq. (20), using a modified Euler's method. Denoting the right-hand side of Eq. (20) at jth location and nth time as $J(U^n_j)$, the modified Euler's method involves predictor–corrector steps similar to the first-order Euler's method, where the conservative variable U_j at $t^n + \Delta t$ is calculated by averaging its value at the end of the two steps.

$$U^{*}_j = U^n_j + \Delta t \cdot J(U^n_j) \qquad \text{(Predictor)}$$
$$U^{**}_j = U^{*}_j + \Delta t \cdot J(U^{*}_j) \qquad \text{(Corrector)}$$
$$U^{n+1}_j = 0.5 \cdot (U^n_j + U^{**}_j) \qquad \text{(Averaging)} \tag{25}$$

The above integration strategy, being second-order accurate in time, makes the overall numerical scheme second-order accurate in both space and time. It follows from Eqs. (20–24) that, for updating a grid node in time, information at two upstream and two downstream nodes is required. Thus, the central-difference-based numerical scheme can be implemented only at the so-called internal nodes that are not on the rotor–stator interfaces or the external boundaries with the ambient. At points adjacent to interfaces and boundaries, we replace the KT scheme with the three-point central difference Lax–Friedrichs (LxF) scheme, which in semidiscretized form can be written as

$$\frac{\partial U_j}{\partial t} = -\frac{H_{j+1} - H_{j-1}}{2\Delta m_{j,c}} + Q(U_j) \tag{26}$$

The numerical flux H in this case is same as the physical flux F and does not require any reconstruction step, which implies that

$$H_{j+1} = F(U_{j+1})$$
$$H_{j-1} = F(U_{j-1}) \tag{27}$$

On the boundary node itself, the LxF scheme is replaced by one-sided two-points gradient that is part of the boundary scheme explained below.

B. Compact Interface Elements and External Boundaries

The partial differential Eqs. (12–14) governing the flow dynamics inside a compressor are applied within the computational domains of rotors and stators. Between each of two domains, an interface is required to accommodate frame transformation, shock waves, turning losses, and other losses such as mixing losses. Additionally, the interface between the blade rows accommodates for bleed from the compressor. The theory and implementation of this interface is described below.

1. *Characteristics Methods*

There are three characteristic velocities associated with one-dimensional Euler equations:

$$\lambda_1 = V - c$$
$$\lambda_2 = V$$
$$\lambda_3 = V + c \tag{28}$$

Corresponding to the three velocities are three waves, as shown in Fig. 5, whose amplitudes can be calculated using the following relations:

$$L_1 = \lambda_1\left(\frac{\partial p}{\partial m} - \rho c\frac{\partial V}{\partial m}\right)$$
$$L_2 = \lambda_2\left(c^2\frac{\partial \rho}{\partial m} - \frac{\partial p}{\partial m}\right)$$
$$L_3 = \lambda_3\left(\frac{\partial p}{\partial m} + \rho c\frac{\partial V}{\partial m}\right) \tag{29}$$

Note that, in case of supersonic flow, all characteristics point along the same direction. With the above definitions, Euler equations including stream tube area variation and source terms assume the following form:

$$\frac{\partial}{\partial t}(\rho A) = -(\rho V)\frac{\partial A}{\partial m} - \frac{A}{c^2}\left(L_2 + \frac{1}{2}(L_1 + L_3)\right) \tag{30}$$

$$\frac{\partial}{\partial t}(\rho V A) = -(\rho V^2)\frac{\partial A}{\partial m} - \frac{A}{c^2}\left(\lambda_2 L_2 + \frac{1}{2}(\lambda_1 L_1 + \lambda_3 L_3)\right)$$
$$+ (\rho A \Omega^2 r \cos\beta \sin\gamma) - C_f(\rho V^2 b) \tag{31}$$

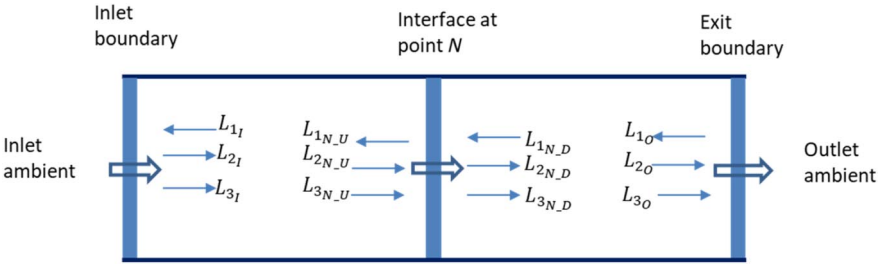

Fig. 5 Direction of characteristic waves at the domain boundaries.

$$\frac{\partial}{\partial t}(\rho e_0 A) = -(\rho V e_0)\frac{\partial A}{\partial m} - \frac{A}{2}\left(\begin{array}{l}\frac{L_1}{\lambda_1}\left(\frac{\gamma V - c}{\gamma - 1} + \frac{1}{2}\frac{V^2}{c^2}(V - 3c)\right) + \frac{L_2}{\lambda_2}\frac{V^3}{c^2} \\ \quad + \frac{L_3}{\lambda_3}\left(\frac{\gamma V + c}{\gamma - 1} + \frac{1}{2}\frac{V^2}{c^2}(V + 3c)\right)\end{array}\right) + (\rho V A \Omega^2 r \cos\beta \sin\gamma) - C_Q \tag{32}$$

Poinsot and Lele [20] established a boundary condition scheme based on characteristics to obtain explicit algebraic connections between the characteristics in specific boundaries. To meet the challenges associated with our problem, however, we need to define the problem in quite general terms that should be implementable in any possible scenario, while entirely independent of the numerical scheme that is used in the internal points of the computational domain.

2. *Interdomain Interface*

As already noted, the flow transformation between two neighboring elements, say, rotor 1 and stator 1, does require not only change of frame, but also the inclusion of shock wave losses and more. Thus, the transformation over the interface is highly nonlinear. However, it turns out that a straightforward method can be devised to solve any transformation regardless of its complexity. Toward that end, consider an interface at grid point N as shown in Fig. 5.

Following Poinsot and Lele [20], we calculate the characteristics that are coming from the domain based on one-sided spatial derivatives and use these to determine the characteristics that enter the domain. The algorithm for this process proceeds along the following steps:

1) Calculate $L_{2_{N\_U}}$, $L_{3_{N\_U}}$, and $L_{1_{N\_D}}$ from Eqs. (28) and (29) using one-sided gradients.

2) Guess a value for $L_{1_{N\_U}}$ (alternatively, one may select the previous value of $L_{1_{N\_U}}$).

3) Find the time derivatives of the upstream state variables $(\partial/\partial t)(\rho A)_{NU}$, $(\partial/\partial t)(\rho VA)_{NU}$, and $(\partial/\partial t)(\rho e_0 A)_{NU}$ by substituting the values of $L_{1_{N\_U}}$, $L_{2_{N\_U}}$, and $L_{3_{N\_U}}$ from steps 1 and 2 in Eqs. (30–32).

4) Integrate $(\partial/\partial t)(\rho A)_{NU}$, $(\partial/\partial t)(\rho VA)_{NU}$, and $(\partial/\partial t)(\rho e_0 A)_{NU}$ from step 3 in time to obtain estimates of the upstream states for the next time step, i.e., $(\rho A)_{NU}(t + \Delta t)$, $(\rho VA)_{NU}(t + \Delta t)$, and $(\rho e_0 A)_{NU}(t + \Delta t)$.

5) Calculate the reference frame transformation, including bleed and losses to obtain downstream state variables $(\rho A)_{ND}$, $(\rho VA)_{ND}$, and $(\rho e_0 A)_{ND}$ at $t + \Delta t$.

6) Subtract current downstream state variables from their estimated values at $t + \Delta t$ from step 5 and divide by Δt to obtain $(\partial/\partial t)(\rho A)_{ND}$, $(\partial/\partial t)(\rho VA)_{ND}$, and $(\partial/\partial t)(\rho e_0 A)_{ND}$.

7) Solve Eqs. (30–32) for $L_{1_{ND}}, L_{2_{ND}}$, and $L_{3_{ND}}$, using $(\partial/\partial t)(\rho A)_{ND}$, $(\partial/\partial t)(\rho VA)_{ND}$, and $(\partial/\partial t)(\rho e_0 A)_{ND}$ from step 6.

8) Compare the calculated $L_{1_{N\_D}}$ from step 7 with its known value obtained in step 1, and correct the guess on $L_{1_{N\_U}}$ in step 2 using the Newton–Raphson or a bisection method.

9) Go to step 3 and iterate the process until convergence is achieved.

3. *Inlet Boundary Compact Interface*

The inlet to the computational domain may be isentropic or may be prefaced by a compact module that accounts for inlet shock waves during high speed operations, or losses due to flow distortion from screens that are often installed at the compressor inlet during static tests. These effects are assumed to be accounted for by an inlet compact interface module (ICIM) that interfaces the first grid point of the computational domain with the ambient. Note that the ambient stagnation conditions just ahead of the ICIM are known at all times though they are not necessarily constant. The following iterative procedure describes the solution process for the inlet boundary:

1) Calculate L_{1_I} from Eqs. (28) and (29) using the one-sided gradient.

2) Guess a value for Mach number just ahead of the ICIM for the next time step $t + \Delta t$ (alternatively, one can use its value from the previous time step).

3) Assuming isentropic flow upstream of the ICIM, calculate pressure, temperature, density, and velocity at the upstream end of the ICIM at $t + \Delta t$ based on the known ambient stagnation conditions and the assumed Mach number in step 2.

4) Calculate values for ρA, ρVA, and $\rho e_0 A$ at the downstream end of the ICIM at $t + \Delta t$ using the ICIM "transfer function." In this paper, the transfer function of the ICIM is set to unity, representing a lossless inlet.

5) Subtract the previous states ρA, ρVA, and $\rho e_0 A$ at time t from the computed values at time $t + \Delta t$ from step 4, and divide the difference by Δt to obtain the values of the time derivatives $(\partial/\partial t)(\rho A)_I$, $(\partial/\partial t)(\rho VA)_I$, and $(\partial/\partial t)(\rho e_0 A)_I$ at the downstream end of the ICIM.

6) Solve Eqs. (30–32) for L_{1_I}, L_{2_I}, and L_{3_I}, using $(\partial/\partial t)(\rho A)_I$, $(\partial/\partial t)(\rho VA)_I$, and $(\partial/\partial t)(\rho e_0 A)_I$ from step 5.

7) Compare the calculated L_{1_I} from step 6 with its known value obtained in step 1, and correct the guess on Mach number made in step 2 using the Newton–Raphson or a bisection method.

8) Go to step 3 and iterate the process until convergence is achieved.

4. *Exit Boundary Compact Interface*

Similar to the ICIM in the inlet, we include an exit compact interface module (ECIM) at the exit of the computational domain. There are several types of exit conditions that the ECIM may accommodate. To name a few, we may have i) a hard termination where flow velocity vanishes at the exit boundary, ii) anechoic termination with no reflection of waves at the exit boundary, iii) discharge into a large plenum, and iv) discharge through a throttle. Each of these cases requires a different formulation of the ECIM transfer function. As an example, we consider here two exit conditions. The first has a lumped plenum coupled to the exit of the computational domain with the plenum pressure p_{pl} forcing the static pressure at the exit of the computational domain. The time derivative of the plenum pressure $\dot{p}_{pl}$ is calculated from a separate set of equations that account for the net balance of mass flux and energy flux into and out of the plenum. The second example of exit condition is a compact throttle with area $A_{\text{th}} < A_e A_{\text{th}} < A$ e discharging to the ambient. The following iterative procedure describes the solution process for the compact interface at the exit boundary:

1) Calculate L_{2_o} and L_{3_o} from Eqs. (28) and (29) using one-sided gradients.

2) Guess a value for L_{1_o} (alternatively, one may select the previous value of L_{1_o}).

3) Insert the values of L_{1_o}, L_{2_o}, and L_{3_o} from steps 1 and 2 in Eqs. (30–32) to calculate the time derivatives of the states $(\partial/\partial t)(\rho A)_o$, $(\partial/\partial t)(\rho VA)_o$, and $(\partial/\partial t)(\rho e_0 A)_o$.

4) For the lumped plenum case, use the time derivatives of the states from step 3 to calculate the time derivative of the pressure $(\dot{p}_e)$ and compare it to the time derivative of the plenum pressure $(\dot{p}_{pl})$. The difference between $\dot{p}_{pl}$ and $\dot{p}_e$ forms the error to be driven toward zero through the iterative process. In the case of a throttle, we first calculate the pressure and Mach number at the throttle opening using isentropic acceleration from the exit A_e to the smaller area A_{th} of the throttle. The boundary condition requires that either the static pressure at the throttle equals the ambient pressure, or else the Mach number at the throttle opening A_{th} equals 1; the latter implies a choked throttle.

5) Using the error from step 4, obtain a new guess for L_{1_o} in step 2 using the Newton–Raphson or a bisection method.

6) Go to step 3 and iterate the process until convergence is achieved.

C. Results and Discussion

In this section, we present unsteady flow simulations for an industrial four-stage axial compression system considered in [14].

A sketch of the geometry of the simulated compressor is shown in Fig. 6.

In the nominal configuration, stator 4 discharges into a plenum that is interfaced to the ambient through a throttle. With the plenum, the B-parameter is calculated to be roughly 0.94. We also consider the case where throttle is connected to the exit of stator 4 via a short duct; however, due to brevity, these results are not discussed here. As such, all results presented in this paper are with a plenum, and they include transitions to choke as well as stall.

The inclusion of a "large" plenum in a 1-D scheme may be done in two ways. If the plenum has large-enough ratio of length-to-flow area, it can be included as part of the wave guide passages in the scheme with proper interface to the compressor on one side and throttle on the other side. Otherwise, the plenum can be evaluated as a lumped volume in which velocity is negligible and pressure is uniform throughout the volume. In the results shown below, the first approach is taken; thus wave propagations inside the plenum are present.

1. *Stability of the Numerical Scheme and Mass Conservation Considerations*

As already discussed, the KT scheme employs two grid points ahead and two grid points behind the center point. This scheme, thus, cannot be employed at grid points that are at or next to interfaces. Hence, we switch to an alternate scheme as the simulation approaches one of the interfaces; note that there are two interfaces for each compact zone and one interface each at the inlet or exit of the system. As already noted, at the grid point next to an interface we switch to the three-point central difference LxF scheme [see Eq. (26)] that uses the interface grid point as the front (rear) point. At the interface grid point, we use the one-sided backward (forward) gradient. Although changing schemes near the interfaces did not give rise to any numerical stability issues in our simulations, we observed spurious spatial oscillations at grid points near the interface boundaries in some of the cases. While such oscillations were observed to die out within a few grid points, we noticed small residual imbalances in the mass flux across some of the interface boundaries. However, we found the overall mass flux imbalance to be negligibly small in all the cases considered in this study.

2. *Grid Resolution Considerations*

In our estimation of error due to grid spacing, we have chosen to run the simulation code at conditions of deep choke when multiple shock waves develop in the rotors. Table 1 shows the computed values of the normalized exit pressure ratio $\bar{P}_R$ obtained from simulations for different values of grid spacing along the mean line, Δm, in millimeters.

It is expected that computational error varies monotonically as an exponent of grid spacing. Hence, in order to estimate percentage error in the computed normalized exist pressure ratio for a selected value of the grid spacing, we assume a model for the estimated normalized pressure ratio ($\widehat{\bar{P}_R}$) as a function of the grid spacing as

$$\widehat{\bar{P}_R}(\Delta m) = \bar{P}_{R\Delta m\to 0} + K(\Delta m)^{\varepsilon} \tag{33}$$

where $\bar{P}_{R\Delta m\to 0}$ is the "computationally correct" value of the normalized pressure ratio as grid spacing $\Delta m \to 0$, which is unknown at this point. Also, K and ε in Eq. (33) are unknown parameters to be determined. We have used the least-square method to fit the Table 1 data to Eq. (33) and estimated the values of unknown parameters as $\bar{P}_{R\Delta m\to 0} = 0.94385$, $K = 0.06723$, and $\varepsilon = 0.79209$. Next, we obtain an estimate of the error for a selected value of grid spacing Δm.

Table 1 Exit pressure ratio for different values of grid spacing

Grid spacing, Δm (mm)	Normalized exit pressure ratio, $\bar{P}_R$
0.8	1.0
0.4	0.9773
0.2	0.9614
0.1	0.9553

$$\hat{E}(\Delta m) = \frac{\bar{P}_R(\Delta m) - \bar{P}_{R\Delta m\to 0}}{\bar{P}_{R\Delta m\to 0}} \tag{34}$$

A plot of Eq. (34) is shown in Fig. 7 using the estimated parameter values of Eq. (33). The error estimates for the data in Table 1 are also superimposed as square symbols in Fig. 7. All the results using the unsteady simulation code included in this paper are with the grid spacing Δm of 0.2 mm, which, from Fig. 7, corresponds to an estimated error of roughly 2%.

3. *Throttling into Choke*

Figure 8 shows the progression from an initial stable point toward and into the choked branch. The initialization state for simulation corresponding to the steady-state points shown in this figure, as well as those shown in other figures latter, is calculated using an initialization routine briefly described below.

In the initializer routine, a flow rate is set and the pressure distribution along the compressor is calculated. The required throttle area is calculated as part of the initializer routine. The calculated flow spatial distribution and throttle opening are subsequently used as the initial condition in the time marching scheme. After an initial settling

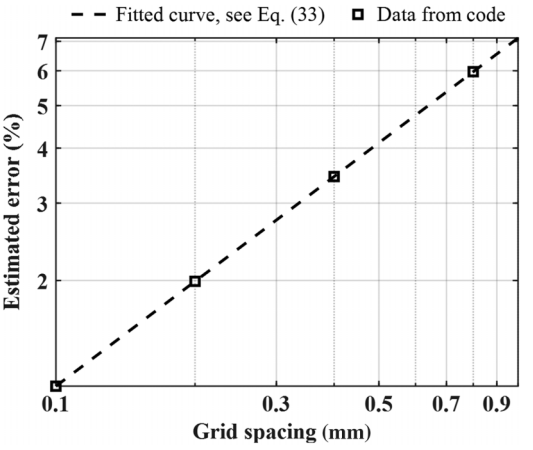

Fig. 7 Estimated error for different values of grid spacing.

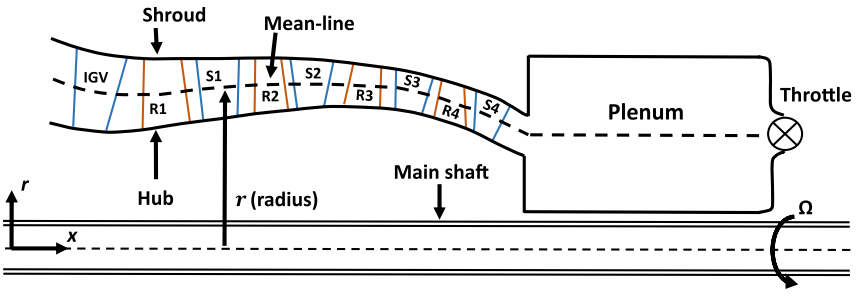

Fig. 6 Geometry of the simulated compressor.

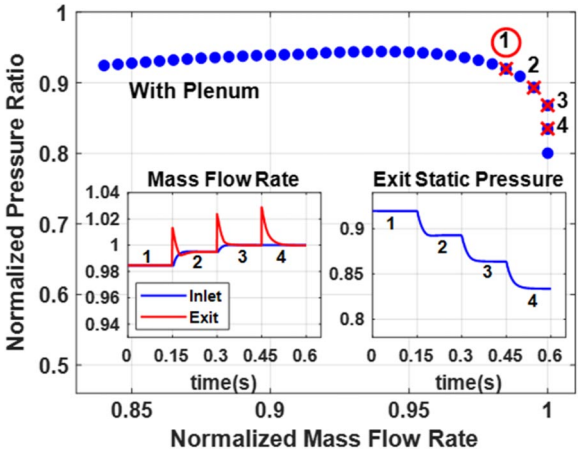

Fig. 8 Mass flow rate and static pressure response at 100% speed for throttling from operating points 1 to 4 showing flow choking at operating points 3 and 4.

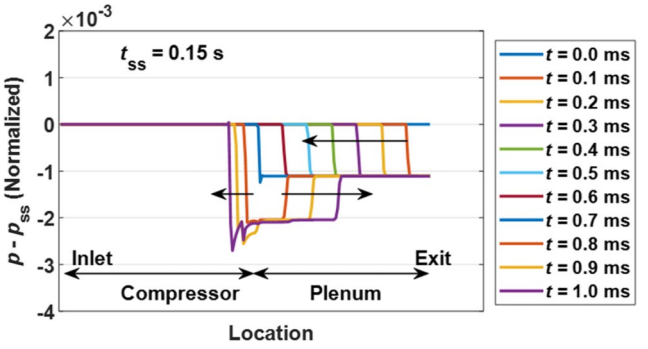

Fig. 9 Time snapshots of pressure wave front from 0 to 1 ms presented as deviations from the steady state due to throttling from point 1 to point 2 (see Fig. 8) toward choke.

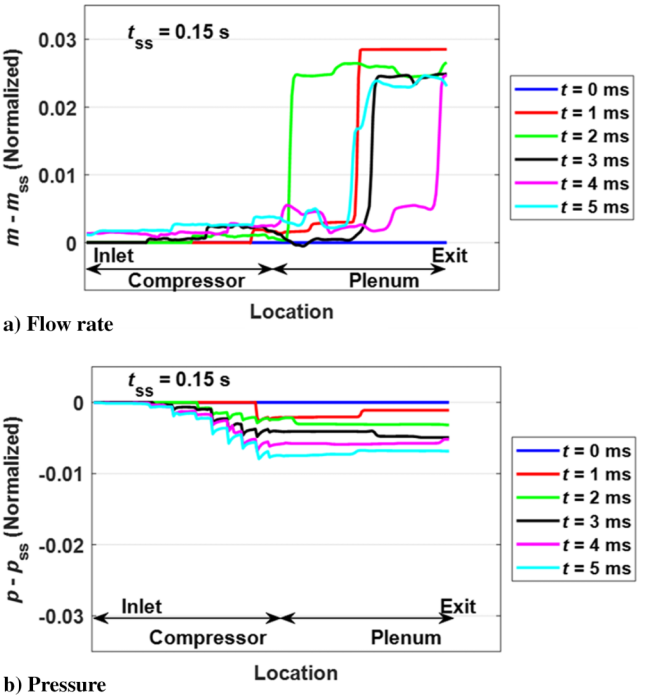

Fig. 10 Snapshots of mass flow rate and pressure deviations from steady state at different times during 0–5 ms following throttling from point 1 to point 2 (see Fig. 8) toward choke.

time in which any small deviations from the calculated steady state are settled, the throttle is switched to a 2% area increase followed by another settling period. This process is repeated three times. Points 1 and 2 in Fig. 8 are on the part of the characteristics in which the flow is not choked at any location along the compressor; points 3 and 4 in Fig. 8 are on the choked branch where one or more stages experience choking conditions. The time traces of the mass flow rate at the inlet and exit show that, for each throttle change, the mass flow rate at the throttle surges up and subsequently settles down, whereas the flow rate at the inlet grows gradually, eventually matching the flow rate at the exit. For the switch from point 3 to point 4, the flow at the inlet experiences no change and the flow at the exit overshoots initially, but eventually settles to the flow rate of the previous throttle setting, indicative of a choked state.

We now look into the details of the wave structure in the plenum and the compressor section. The area ratio of the plenum to the compressor exit is about 13:1, large enough to represent a near-solid wall to waves impinging from the plenum side and an open end for waves approaching from the compressor side. Also, the choked throttle at the plenum exit is nearly a solid termination for the impinging waves. The low Mach number and the combination of temperature and length in the plenum imply that about 2/3 of a millisecond is needed for a wave, moving at the speed of sound, to traverse the plenum in each direction. However, once the wave enters the compressor from the back, it is significantly slowed down by the opposing mean flow velocity in the compressor passages so that it takes about 3 ms for a wave to traverse the distance from the throttle to the inlet.

To be able to follow the relatively small variations in the pressure and flow rate that follow the throttle switch, we show the incremental difference from the previous steady state. This should be kept in mind while reviewing the following figures. Accordingly, at $t = 0$ ms the blue line is uniformly at zero.

Figure 9 shows the wave formation dynamics following the first millisecond after the throttle is stepped from 1 to 2. It shows a steep expansion wave moving from the throttle to the left and reaching the interface with the compressor in about 0.75 ms. The impinging expansion wave is partially reflected as an expansion wave and partially transmitted into the compressor. Because of the high area ratio, the reflection is almost full as evident by the near doubling of the amplitude of the reflected wave. Note that the transmitted pressure wave has essentially the same amplitude as the reflected wave.

Figure 10 shows snapshots sequence during 0–5 ms of the spatial distributions of flow rate and static pressure, immediately following the throttle switch from point 1 to point 2 toward choke. As already shown for the duration of 1 ms after the switch, the red line corresponding to $t = 1$ ms shows that the expansion wave that originated at the throttle opening and caused a rush of flow at the exit has moved through the plenum into the compressor, and partially reflected as an expansion wave that has already traveled half of the plenum back toward the throttle. One millisecond later at $t = 2$ ms, the expansion wave has already impinged on the throttle side and reflected also as an expansion wave, almost reaching the compressor interface, shown as the green line. Meanwhile, the initial wave inside the compressor keeps propagating toward the inlet, also shown in the green line. At $t = 3$ ms, the wave front has impinged on the interface, moved back as an expansion wave and reflected back from the throttle side again propagating into the plenum as an expansion wave, the front of which is evident as the black line nearing the middle of the plenum. By $t = 4$ ms, the front of the black line has already impinged on the compressor interface, traveled back, and is just about to impinge on the throttle side, shown as the magenta line. This process continues with ever so diminishing wave amplitude and gradually decreases the plenum pressure. While the waves are bouncing in the plenum, they are of course affecting the flow in the compressor too. From the flow rate results, it can be seen that at $t = 3$ ms(black line), the front of the initial wave has not yet reached the inlet. By $t = 4$ ms, the wave front has reached the inlet as evident by the change in flow rate at the inlet (magenta line).

Figure 11 shows the interval of 45–50 ms following the throttle switch from point 1 to point 2. It shows that the compressor has nearly

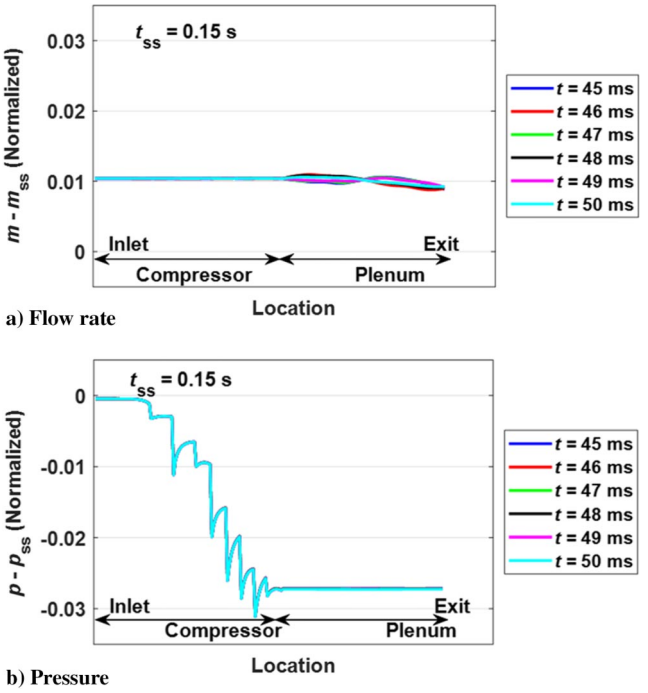

Fig. 11 Snapshots of mass flow rate and pressure deviations from steady state at different times during 45–50 ms following throttling from point 1 to point 2 (see Fig. 8) toward choke.

settled at the new operating condition but for small deviation shown in the flow rate in the plenum. Interestingly, it can be seen that, while the pressure in the plenum is nearly uniform, the mass flow rate distribution in the plenum is not fully settled and it oscillates in fundamental longitudinal acoustic mode having nodes at the choked throttle on one side and the large area ratio interface on the other side. From the simulation results for the interval of 90–100 ms after the throttle switch from point 1 to point 2 shown in Fig. 12, it is seen that the compressor has reached the new steady state as all lines have converged.

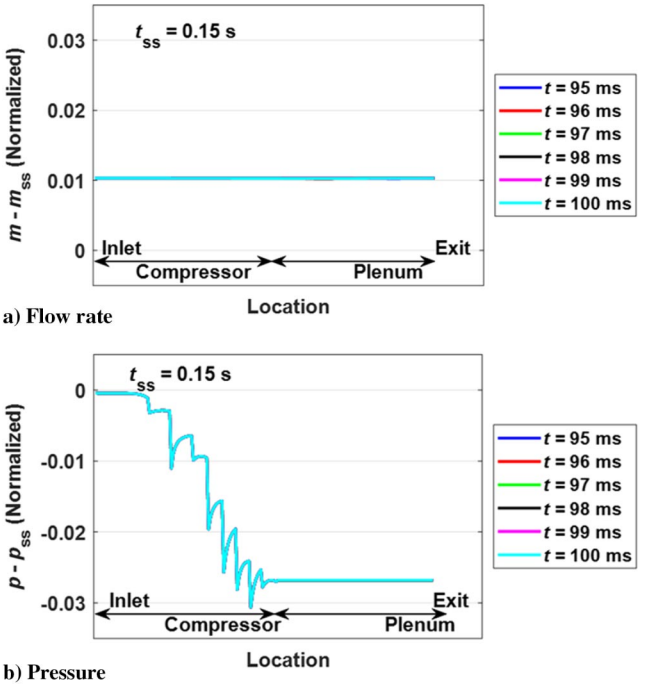

Fig. 12 Snapshots of mass flow rate and pressure deviations from steady state at different times during 95–100 ms following throttling from point 1 to point 2 (see Fig. 8) toward choke.

Simulation results for the scenario following the switch from point 3 to point 4 (see Fig. 8) for the intervals of 0–5 ms and 90–95 ms are shown in Figs. 13 and 14, respectively. The results are very similar to the results for the switch between points 1 and 2 discussed above, but with one difference. In this case, the front half of the compressor experiences no change in pressure and/or mass flow rate, indicating the location of the choking point that occurs to be the inlet to stator 1.

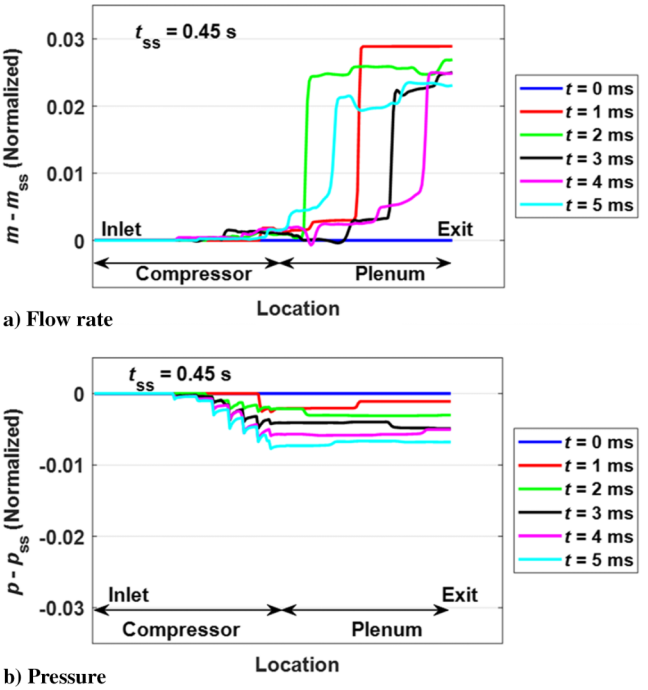

Fig. 13 Snapshots of mass flow rate and pressure deviations from steady state at different times during 0–5 ms following throttling from point 3 to point 4 (see Fig. 8) in choke.

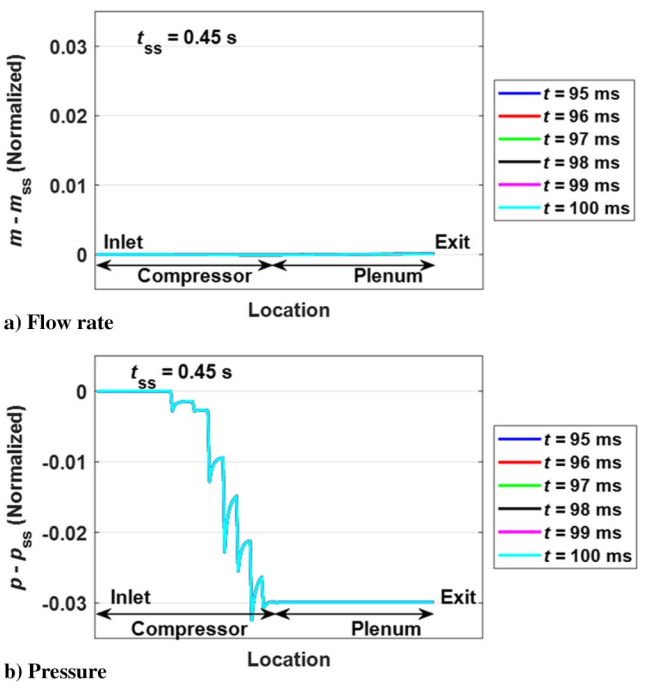

Fig. 14 Snapshots of mass flow rate and pressure deviations from steady state at different times during 95–100 ms following throttling from point 3 to point 4 (see Fig. 8) in choke.

4. Throttling into a Modal Stall

We turn our attention now to the throttling schedule shown in Fig. 15. Stall is initiated by gradually changing compressor operation from negative to positive slope on the compressor characteristics, allowing longitudinal and circumferential modes to grow. Accordingly, this kind of stall is commonly denoted as modal stall, even though, strictly speaking, there are no modes in our mean line model. In this run, mass flow rate decreases as the throttle is closed in steps and pressure increases until in the last step the compressor loses stability, resulting in ever so escalating drop in the pressure and flow rate.

Figure 16 shows the high-resolution time snapshots of the pressure structure in the first 1 ms after the throttle step from point 1 to point 2. It is similar to the previous scenario but for the fact that the waves are now compression rather than the expansion waves.

Figure 17 shows the corresponding snapshots of the waves following the switching from point 1 to point 2 during the first 5 ms. The scenario is very similar to the case of throttle opening in the unchoked side discussed above. We leave it to the reader to follow the back-and-forth motion of the waves. Also, similar to the response of throttle opening, at the end of the first 5 ms, the flow through the plenum is still vastly different from the flow through the compressor. However, it could be understood that 100 ms later the flow rate through the plenum perfectly matches with that of the compressor. Note that those figures are not shown for the sake of brevity.

We now turn to analyze the critical switch from point 3 to point 4 (see Fig. 15) that ends ultimately with a loss of stability. The behavior during the first 5 ms is shown in Fig. 18. The pressure plot shown in Fig. 18 is very similar to that shown for the switch from point 1 to point 2 in Fig. 17. However, in the flow rate plot shown in Fig. 18, the $t = 5$ ms trace (cyan line) shows that the flow rate through the compressor is dropping in an accelerated rate in comparison to that for the throttle switch from point 1 to point 2 shown in Fig. 17.

Plots of the traces during 6–10 ms after the switch from point 3 to point 4, shown in Fig. 19, confirm that the flow through the compressor is dropping in ever-increasing fashion, even as the pressure ratio still increases across the compressor. This divergence ultimately

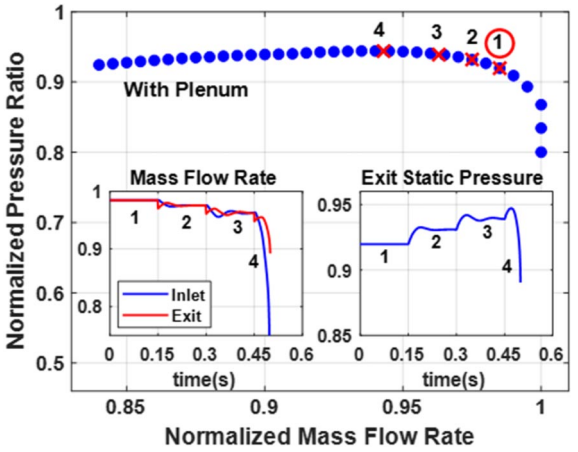

Fig. 15 Mass flow rate and static pressure response at 100% speed for throttling from operating points 1 to 4 showing stall between points 3 and 4.

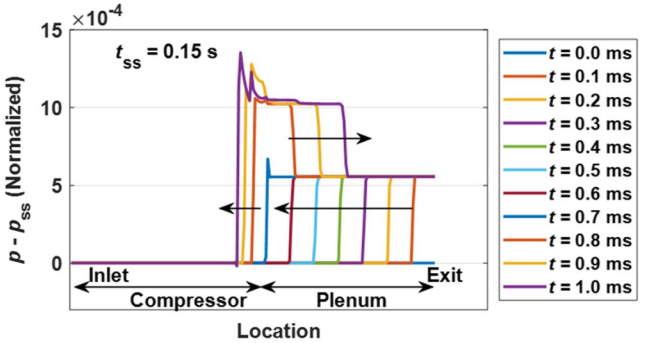

Fig. 16 Time snapshots of pressure wave front 0 to 1 ms presented as deviations from the steady state during throttling from point 1 to point 2 (see Fig. 15) toward stall.

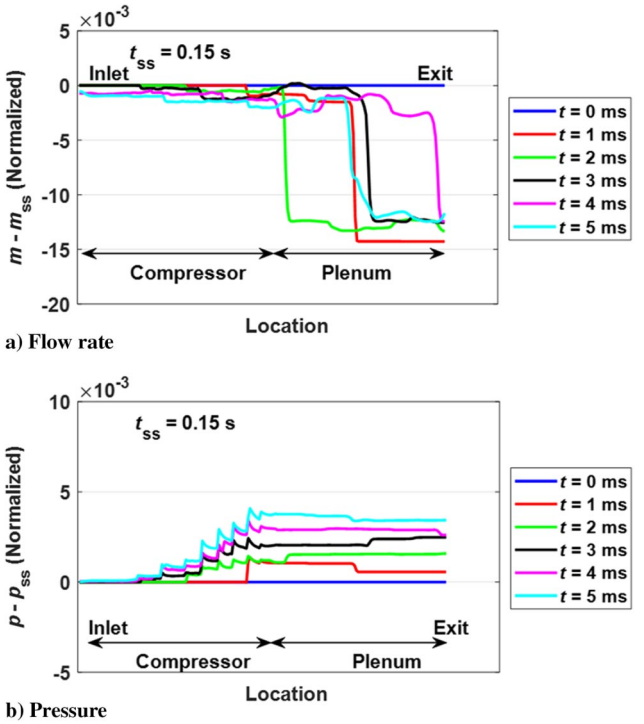

Fig. 17 Snapshots of mass flow rate and pressure deviations from steady state at different times during 0 = 5 ms following throttling from point 1 to point 2 (see Fig. 15) toward stall.

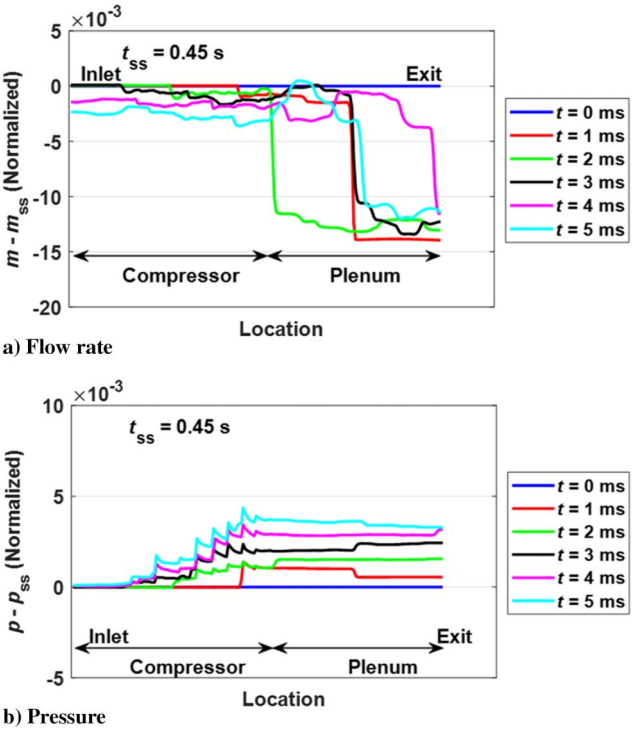

Fig. 18 Snapshots of mass flow rate and pressure deviations from steady state at different times during 0–5 ms following throttling from point 3 to point 4 (see Fig. 15) toward stall.

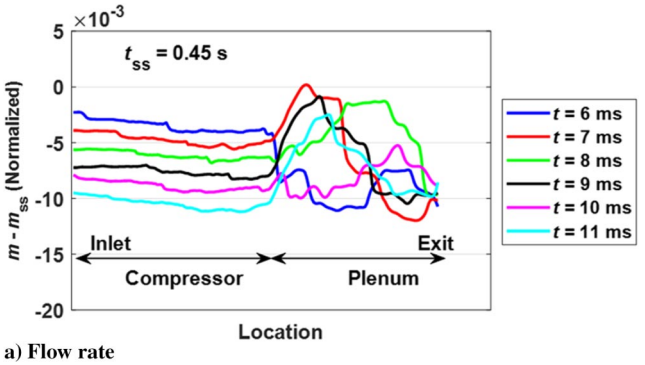

a) Flow rate

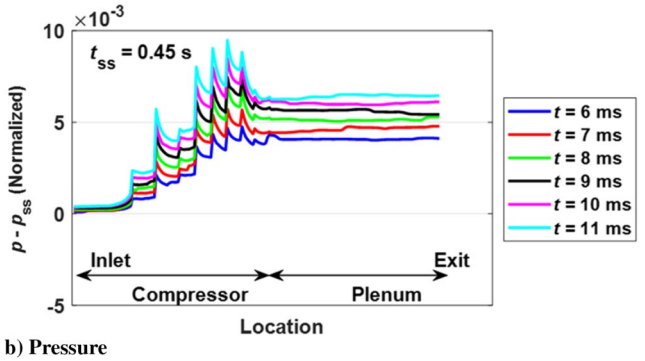

b) Pressure

Fig. 19 Snapshots of mass flow rate and pressure deviations from steady state at different times during 6–10 ms following throttling from point 3 to point 4 (see Fig. 15) toward stall.

leads to a flow reversal at $t = 49.5$ ms corresponding to the beginning of surge (see Fig. 20). Notably, from an examination of the last millisecond of simulation in the stall process, it can be seen that pressure in the middle of the compressor is rapidly increasing, whereas at the back of the compressor, it is rapidly decreasing. This kind of behavior is commonly observed in real tests, and it is often inferred as an indication that the compressor stalled somewhere near the back. However, the inference from test data of "stalled in the back" can be wrong as illustrated in this simulation example of a midsection stall. This observation underscores the usefulness of the developed model as a diagnostic tool for proper interpretation of test data.

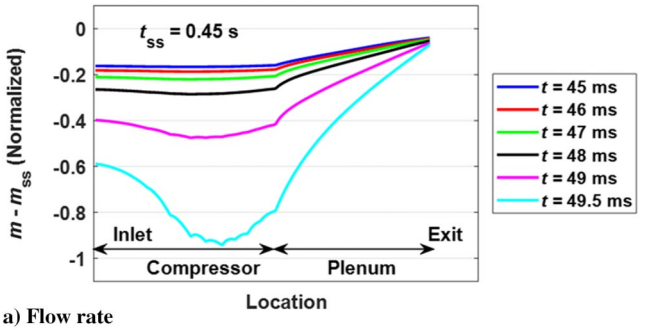

a) Flow rate

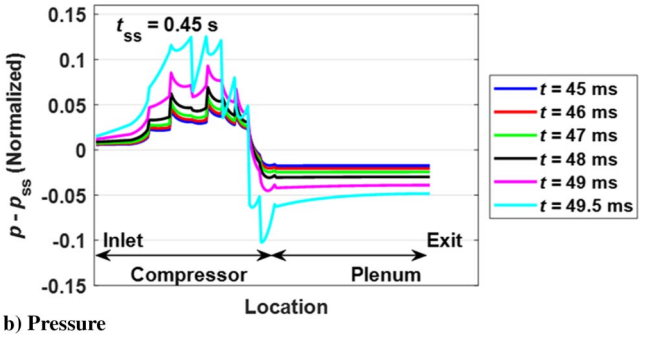

b) Pressure

Fig. 20 Snapshots of mass flow rate and pressure deviations from steady state at different times from 45 ms onward following throttling from point 3 to point 4 (see Fig. 15) toward stall.

It is important to note that the initial gradual flow divergence during the first 10 ms is manifested almost uniformly along the compressor, thus indicating that flow in the compressor responds mostly as a bulk. This suggests that the wave motion across the compressor has little to do with the mechanism that is responsible for the initial divergence. In essence, the behavior of the system follows more or less the compressor dynamics described by Greitzer's model [4,5]. Accordingly, the loss of stability that occurs once the overall characteristics of the compressor are near its peak is associated with the B-parameter, which increases with the plenum volume. Thus, one may expect that the dynamics of the compressor would be significantly altered if the plenum is eliminated and a throttle is attached at the exit of the last stator or in its vicinity. This indeed was confirmed in our simulations using the developed model. However, simulation results for the "no plenum" case are not included for brevity.

5. *Throttling into Spike Stall*

The loss of stability discussed so far is manifested when a compressor is transitioned gradually from the negative slope side to the positive slope slide of its characteristic. Such a situation is more likely to happen in a compressor where all the stages are matched so that all stages move toward the individual stage peak pressures together. This stall type is akin to the "modal stall" discussed by Camp and Day [21]. However, when the stages are not well matched, it can happen that an individual stage is well into the left of its peak (positive slope) while the overall compressor is still on the negative slope side of its characteristic. In such a case, the so-called spike stall may occur in the stage that crosses its peak, and it can drag the overall system into stall even when it is operating in the right side of the global characteristic. This situation was discussed by Camp and Day [21]. It is expected that this case leads to a stall process with different dynamics than that associated with a modal stall process shown in Figs. 15–20.

To simulate the case where a compressor can exhibit loss of stability due to the so-called spike stall, we introduce a step change in blade row losses due to incidence if the angle of attack of any blade row increases above 17 deg. This abrupt change in individual blade row losses emulates a sudden flow separation, which in turn can cause an abrupt change in flow dynamic response. The resulting steady-state characteristic (marked as modified) is shown in Fig. 21. The inset plots shown in Fig. 21 are the time traces of mass flow rate and compressor exit pressure as the system is throttled in steps from point 1 to point 2, and then from point 2 to point 3. It is notable that the spike is triggered just to the left of point 3, which is still on the stable branch. Further, it can be seen that the modified branch point 3′ has a

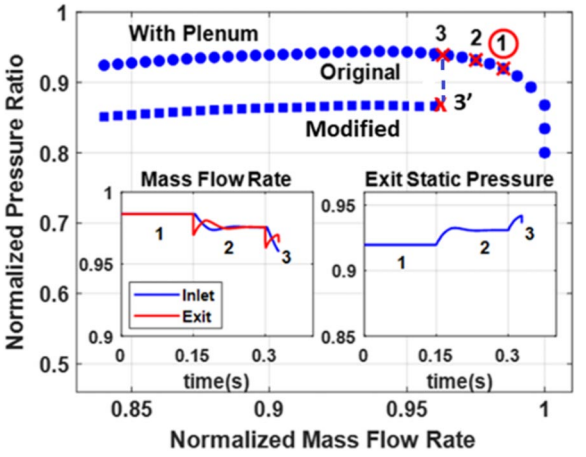

Fig. 21 Mass flow rate and static pressure response at 100% speed for the case of stall showing loss of stability to the right of peak pressure when stator 4 crosses the set stall angle of attack.

negative slope as well, thus opening up the possibility that the system may not collapse to surge even after a blade row experiences a spike stall. Since a fully developed spike stall is manifested as a local rotating perturbation, a compressor can exhibit a limit cycle pressure oscillation without collapsing to surge. Such cases are reported in [21]. However, when the jump in the characteristic is large enough, as it is with the results shown in Fig. 21, the ensuing transient will not "allow" the compressor to regain stability, thus driving it to surge. It can be seen that when spike stall is not present, such as the case for the results shown in Fig. 15, the system reaches a steady state at point 3 in response to a step change in throttle from point 2. In contrast, when spike stall is present, such as the case for the results shown in Fig. 21, the system is unable to reach a steady state at either point 3 or point 3′ as evident from the inset pressure and mass flow rate plots shown in Fig. 21.

Figure 22 records the pressure and flow distribution snapshots in short intervals past $t = 0.3$ s when a step change in throttle is introduced (see point 2 in Fig. 21). The snapshots with an interval of 0.1 ms start at 27 ms after the throttle change. From the mass flow rate plot in Fig. 22a, it can be seen that at 27.5 ms, a small pulse appears just ahead of stator 4, indicating a spike stall in stator 4. Subsequently, the pulse progresses as a compression front upstream of stator 4 while moving downstream as an expansion front, as evident from the undershoot of the pressure at the back edge of the pulse. Considering that the location of stalling stage is near the plenum, the impression of the expansion wave of pressure is all but unrecognizable once it enters the plenum and travels toward the throttle opening, but is very evident upstream as the compression wave moves toward the compressor inlet. Nevertheless, the dramatic influence on the flow rate is evident at both upstream and downstream of the stalling stage as the negative flow pulse progresses fast into the plenum as well as toward the compressor inlet. The results suggest that an array of stationary pressure sensors in the casing along the compressor can be used to find the stalling stage, as the sensor that first detects a sharp pressure jump indicates the stage that drives the compressor toward loss of stability.

6. *Model as a Diagnostic Tool*

We next present unsteady simulation results to illustrate how the developed model may be important as a diagnostic tool. To that end, we study the case where a compressor crosses to the left side of its peak pressure before a spike stall is initiated. We revisit the modal stall case of Fig. 15, after including in the unsteady model, step changes in losses due to flow separation if any blade row angle of attack increases above 20 deg. Due to this change, the compressor is again stable at point 3. As the compressor is transitioning from point 3 (i.e., right side of its peak pressure) toward point 4 (i.e., left side of its peak pressure) in Fig. 15, it gets into a spike stall while it is simultaneously undergoing a modal stall.

Figure 23a shows the history of pressure readouts from sensors located in the casing along the compressor for the time duration beginning at $t = 0.45$ s when a step change in throttle is given to transition the system from point 3 toward point 4 (see Fig. 15). It can be seen from Fig. 23a that, between 0.45 and 0.47 s, all sensor readings indicate increasing pressure. Past $t = 0.47$ s, some sensors continue recording pressure raise while others record pressure drop, thus suggesting that one or more blade rows are now beyond their peak pressures. The gradual changes in pressure readings end abruptly shortly after $t = 0.495$ s with much sharper changes at the end. It is interesting to note that from the simulation results presented in Fig. 23a, it can be seen that there is a sharp drop in pressure in the reading of the sensor located at the exit of S4, whereas all the remaining sensors see a sharp increase in pressure. It is also interesting to note that even those sensors that show a gradual decrease in pressure almost till the end experience a sharp raise at the end. Figure 23b shows a zoom-in of the sensor readings during the last 2 ms just before a complete collapse occurs. From Fig. 23b, it can be seen that at around $t = 0.4965$ s, the sensor located between R4 and S4 experiences a sharp pressure jump indicating a spike stall in stator 4. This compression wave travels upstream and is detected by the S3-R4 sensor, followed by the R3-S3 sensor. At the same time, an expansion wave moves downstream and is detected by the sensor at the exit of rotor 4. While superficial analysis of the end game could suggest that a spike stall of stator 4 drove the compressor to stall, the reality was that the compressor was already driving itself to stall, and thus the spike stall did not play any role in the stall triggering. This example demonstrates the potential use of the developed unsteady model as a diagnostic tool. The idea here is to simulate the dynamic behavior of the compressor during the tests and use it to "explain" the dynamic data provided by the sensors.

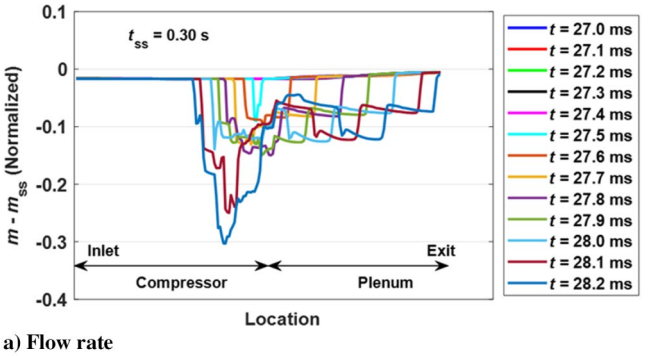

a) Flow rate

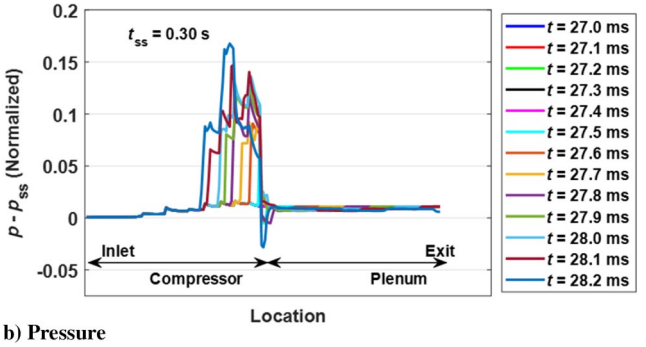

b) Pressure

Fig. 22 Flow and pressure variation distribution just before the spike stall.

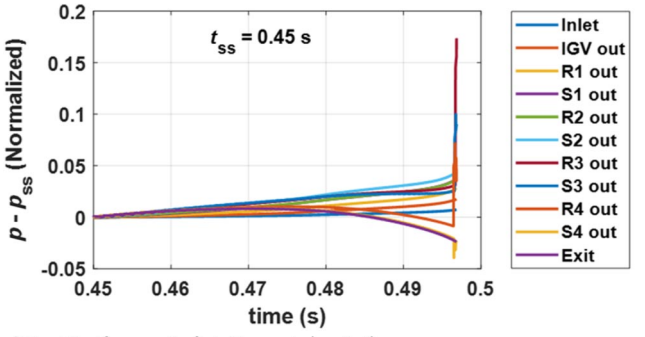

a) Last half second of stall event simulation

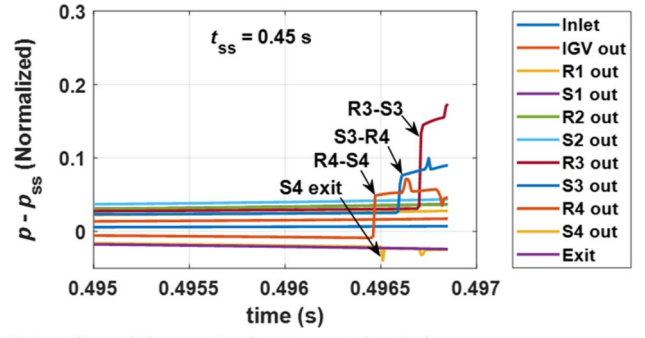

b) Last few milli-seconds of stall event simulation

Fig. 23 Time history of pressure variations at various stages during a stall event.

IV. Conclusions

The paper details the development of a quasi-1-D stream-tube-based dynamic model of unsteady compressible flow along the mean line of a generic compressor comprising both axial and centrifugal stages by modeling stage elements as successive diffusers.

Some of the unique features of the developed model include the following:

1) It models the flow in the respective passages of the cascades taking into account the stagger of the passages.

2) It has no aerodynamic force term in the momentum equation, and the entire dynamics of the flow is captured through the kinetic energy added due to relative rotation between the stages.

3) It has built in loss models that account for, among other things, losses due to incident angles.

4) It uses novel characteristics-based compact interfaces for communication between the neighboring stage elements that take into account the turning losses due to incident angles, and also, facilitate transition into and out of choked conditions of a stage.

A numerical scheme that implemented the model has been shown to be capable of simulating the progression of sharp compression and expansion wave fronts. The ability of the scheme has been demonstrated by predicting the dynamic flow behavior of an industrial four-stage axial compressor. The results show that the scheme successfully generates the acoustic impedance that is responsible for choking. In throttling toward stall, the simulation predicted, as expected, that with large plenum the compressor loses stability when it is driven beyond the peak of its characteristics. Further, the model is shown to be capable of simulating the effect of spike stall in which a compressor stalls at an operating point to the right side (negative slope) of the peak of its characteristic. Lastly, the numerical scheme has been used to simulate response of a pressure sensor array in a test where the compressor experiences a mixed modal and spike stall process. Simulation results are presented, which underscore the potential of the developed model as a diagnostic tool that correlates test results with expected dynamic behavior of a compressor.

The numerical simulation results presented in this paper entailed a mechanical throttle, emulating a core test. However, practical use of the developed model extends well beyond this setup. A short list of potential applications includes 1) dynamic response of the spool and pressure as function of heat addition in the turbine, 2) effect of high-frequency pressure oscillations upon the stability of the machine, 3) effects of bulk and distributed volumes on the stability margin of the compressor, 4) a diagnostic tool, in conjunction with test results, to find out the process through which a compressor loses stability, and 5) effects of heat transfer between the casing and core flow, particularly during hot engine re-acceleration transients, also known as, "Bodie" transients.

Acknowledgments

The authors would like to acknowledge the helpful discussions with the Editor-in-Chief Joseph Powers on the subject of inclusion of dissipative forces in 1-D mean-line flow analysis and on the subject of grid spacing error estimation.

References

[1] Schmidt, J. F., "Off-Design, Computer Code for Calculating the Aerodynamic Performance of Axial Flow Fans and Compressors," NASA CR-198362, July 1995.

[2] Johnson, M. S., "One-Dimensional, Stage-by-Stage, Axial Compressor Performance Model," American Soc. of Mechanical Engineers Paper 91-GT-192, June 1991.
https://doi.org/10.1115/91-GT-192

[3] Veres, J. P., "Axial and Centrifugal Compressor Mean-Line Flow Analysis Method," AIAA Paper 2009-1641, Jan. 2009.
https://doi.org/10.2514/6.2009-1641

[4] Greitzer, E. M., "Surge and Rotating Stall in Axial Flow Compressors—Part I: Theoretical Compression System Model," *Journal of Engineering for Gas Turbines and Power*, Vol. 98, No. 2, April 1976, pp. 190–198.
https://doi.org/10.1115/1.3446138

[5] Greitzer, E. M., "The Stability of Pumping Systems—The 1980 Freeman Scholar Lecture," *Journal of Fluids Engineering*, Vol. 103, No. 2, June 1981, pp. 193–242.
https://doi.org/10.1115/1.3241725

[6] Moore, F. K., "A Theory of Rotating Stall of Multistage Axial Compressors: Part I—Small Disturbances," *Journal of Engineering of Gas Turbines and Power*, Vol. 106, No. 2, April 1984, pp. 313–320.
https://doi.org/10.1115/1.3239565

[7] Longley, J. P., "Calculating Stall and Surge Transients," *Proceedings of GT2007 ASME Turbo Expo 2007: Power for Land, Sea and Air*, American Soc. of Mechanical Engineers Paper GT2007-27378, 2007.
https://doi.org/10.1115/GT2007-27378

[8] Léonard, O., and Adam, O., "A Quasi-One-Dimensional CFD Model for Multistage Turbomachines," *Journal of Thermal Science*, Vol. 17, No. 1, March 2008, pp. 7–20.
https://doi.org/10.1007/s11630-008-0007-z

[9] Dhingra, M., Prasad, J. V. R., Tiwari, P., Nakano, T., and Breeze-Stringfellow, A., "Impact of Inter-Stage Dynamics on Stalling Stage Identification," American Soc. of Mechanical Engineers Paper GT2011-46668, June 2011.
https://doi.org/10.1115/GT2011-46668

[10] Lieblein, S., Schwenk, F. S., and Broderick, R. L., "Diffusion Factor for Estimating Losses and Limiting Blade Loading in Axial-Flow-Compressor Blade Elements," NACA RM E53D01, June 1953.

[11] Lieblein, S., "Experimental Flow in Two-Dimensional Cascades," NASA SP-36, Chapter VI, 1965.

[12] Smith, L. H., and Koch, C. C., "Loss Sources and Magnitudes in Axial Flow Compressors," *Journal of Engineering for Gas Turbines and Power*, Vol. 98, No. 3, July 1976, pp. 411–424.
https://doi.org/10.1115/1.3446202

[13] Denton, J. D., "The 1993 IGTI Scholar Lecture: Loss Mechanisms in Turbomachines," *Journal of Turbomachinery*, Vol. 115, No. 4, Oct. 1993, pp. 621–656.
https://doi.org/10.1115/1.2929299

[14] Mishra, A., Neumeier, Y., Prasad, J. V. R., and James, D. K., "Modelling of Multistage Axial Compressor Using Successive Diffusers with Velocity Sources: Part I—Steady State Results," AIAA Paper 2017-4734, July 2017.
https://doi.org/10.2514/6.2017-4734

[15] Moore, F. K., "A Theory of Rotating Stall of Multistage Axial Compressors: Part I—Small Disturbances," *Journal of Engineering for Gas Turbines and Power*, Vol. 106, No. 2, Apr 1984, 313–320.
https://doi.org/10.1115/1.3239565

[16] Roe, P. L., "Approximate Riemann Solver, Parameter Vectors and Difference Schemes," *Journal of Computational Physics*, Vol. 43, No. 2, Oct. 1981, pp. 357–372.
https://doi.org/10.1016/0021-9991(81)90128-5

[17] Mohanraj, R., Neumeier, Y., and Zinn, B. T., "Characteristic-Based Treatment of Source Terms in Euler Equations for Roe Scheme," *AIAA Journal*, Vol. 37, No. 4, April 1999, pp. 417–424.
https://doi.org/10.2514/2.749

[18] Lax, P. D., "Weak Solutions of Nonlinear Hyperbolic Equations and Their Numerical Computation," *Communications on Pure and Applied Mathematics*, Vol. 7, No. 1, Feb. 1954, pp. 159–193.
https://doi.org/10.1002/cpa.3160070112

[19] Kurganov, A., and Tadmor, E., "New High-Resolution Central Schemes for Nonlinear Conservation Laws and Convection-Diffusion Equations," *Journal of Computational Physics*, Vol. 160, No. 1, May 2000, pp. 241–282.
https://doi.org/10.1006/jcph.2000.6459

[20] Poinsot, T. J., and Lele, S. K., "Boundary Conditions for Direct Simulations of Compressible Viscous Flows," *Journal of Computational Physics*, Vol. 101, No. 1, July 1992, pp. 104–129.
https://doi.org/10.1016/0021-9991(92)90046-2

[21] Camp, T. R., and Day, I. J., "A Study of Spike and Modal Stall Phenomena in a Low-Speed Axial Compressor," *Journal of Turbomachinery*, Vol. 120, No. 3, July 1998, pp. 393–401.
https://doi.org/10.1115/97-GT-526

F. Liu
Associate Editor